Cross slip of extended dislocations in face-centered cubic metals through phase-field modeling

Wise, Ian Paul
Hunter, Abigail
Beyerlein, Irene J.

To be published in: Modelling and Simulation in Materials Science and Engineering

DOI to publisher's version: 10.1088/1361-651X/ade31f

Modelling and
Simulation in Materials
Science and
Engineering

ACCEPTED MANUSCRIPT

Cross slip of extended dislocations in face-centered cubic metals through phase-field modeling

To cite this article before publication: Ian Wise *et al* 2025 *Modelling Simul. Mater. Sci. Eng.* in press https://doi.org/10.1088/1361-651X/ade31f

Cross slip of extended dislocations in face-centered cubic metals through phase-field modeling

Ian Wise[1*], Abigail Hunter[2], and Irene J. Beyerlein[1,3]

[1]Materials Department, University of California, Santa Barbara, Santa Barbara, CA, United States
[2]X Computational Physics Division, Los Alamos National Laboratory, Los Alamos, New Mexico, United States
[3]Department of Mechanical Engineering, University of California, Santa Barbara, Santa Barbara, CA, United States
[*]Corresponding author: wise@ucsb.edu

1 Abstract

Cross slip is a dislocation mechanism that significantly impacts the mechanical behavior of engineering alloys. Here, we advance a 3D phase-field dislocation dynamics (PFDD) mesoscale technique to simulate cross slip across a broad range of face-centered cubic (FCC) metals. The formulation incorporates elastic anisotropy, an FCC numerical grid, and a high-fidelity representation of the entire γ-surface from density functional theory for eight FCC metals and no adjustable parameters or rules. The relaxed core structures under zero stress for all metals are predicted to extend in plane. The analytical model for stacking fault width agrees well with the PFDD result under the assumption of elastic isotropy but overestimates it under elastic anisotropy, when the degree of anisotropy is large. The dynamic simulations are designed to elucidate the material parameters that influence the propensity for cross slip. Whether cross slip occurs under a non-Schmid stress or to bypass a hard obstacle, the critical stress to cross slip scales strongly with the anisotropic energy coefficient for a screw dislocation.

2 Introduction

Dislocation-defect interaction mechanisms are key to understanding the deformation behavior of metals and alloys and developing strategies for strengthening them. One common maneuver dislocations use to bypass defects is cross slip, a process by which a screw-oriented dislocation changes its slip plane [1]. In materials with a face-centered cubic (FCC) structure, cross slip is believed to affect many deformation processes, such as dislocation patterns [2–5], slip band formation [6–10], and stage III hardening in FCC metals [8, 11–13]. The lack of cross slip has been tied to greater likelihood for deformation twinning and vice versa [14–16]. Cross slip is fundamental to many interactions with barriers, such as with nanoprecipitates and interfaces [17–20]. With all else being the same, not all FCC metals have the same propensity for cross slip.

The ease of cross slip in an FCC metal depends on properties of the dislocation core. In FCC structures, dislocation cores are planar, lying on {111}-type planes and extended [21]. Due to the ABC stacking sequence of the FCC system, it is energetically favorable for perfect dislocations of $\mathbf{b} = \frac{a}{2}\langle 110\rangle$ to dissociate into a pair of Shockley partials of $\mathbf{b} = \frac{a}{6}\langle 112\rangle$ separated by an intrinsic stacking fault. The potential energy change associated with this fault is the material intrinsic stacking fault energy γ_{isf}. The extent of the dislocation core varies among FCC metals, due to differences in elastic properties, Burgers vector and energetic surface associated with forming faults on the {111} plane. It has long been expected that the degree to which the screw core is extended is related to the ability for the dislocation cross slip.

Understanding the propensity for cross slip benefits from understanding how cross slip can happen. Evidence of dislocation cross slip has been experimentally observed in FCC metals, usually in reaction to high-strength obstacles or immobile dislocation loops [6, 18, 19, 22, 23]. However, cross slip occurs over length ($\approx$ 1 nm) and timescales that are too short to directly observe the cross slip mechanism using current in-situ experimental methods.

Analytical models for the cross slip process of an extended screw dislocation in an FCC structure have been proposed. Over the years, two have prevailed. The Friedel-

Escaig mechanism states that for cross slip to occur, the Shockley partials gliding on the habit plane will need to constrict, forming a compact dislocation, before transferring to the cross slip plane [24, 25]. Accordingly, the ability for cross slip is related to the energy for the two partials to constrict from their equilibrium separation. Models developed for this constriction energy have suggested that it depends on the isotropic shear modulus μ, Poisson's ratio ν and intrinsic stacking fault energy γ_{isf} [26–29]. An alternative cross slip mechanism is the Fleischer mechanism. Only one Shockley partial undergoes cross slip and leaves an $\frac{a}{6}\langle 110\rangle$ sessile stair-rod dislocation [30]. In this mechanism, the formation energy of the stair-rod dislocation would govern the propensity for cross slip. An analytical model for this formation energy has been proposed, which predicts a direct dependence on μ and γ_{isf} [15].

The length and time scales treated by atomistic techniques are ideal for studying cross slip and testing the processes proposed by analytical models. Molecular dynamics (MD) has been extensively used to simulate the sequence of complex changes in atomic configuration involved in cross slip. To date, MD cross slip studies have primarily focused on either FCC Al, Cu, or Ni [31–37]. In most cases atomistic simulations observe a Friedel-Escaig mechanism. One MD study in Ni, however, showed that the Fleischer mechanism was preferred at short line lengths and high applied shear stress [34]. Further, the applied stress state, namely the relative amount of Schmid stress to Escaig stress, has been shown to affect which cross slip mechanism is preferred [33, 36, 37]. With MD, the activation energies and the critical stresses for cross slip have been calculated at or near absolute zero and elevated temperatures and for different states of stress. Identifying the dependence of material properties, such as γ_{isf}, however, remains to be thoroughly studied using atomistic methods. Usually only one FCC metal is studied. Elucidating the role of material properties on the cross slip would entail studying a group of FCC materials with interatomic potentials of differing levels of accuracy and fitting targets. Further, not all FCC materials have accurate interatomic potentials built for dislocation studies available.

Mesoscale models based on continuum mechanics, such as discrete dislocation dynamics (DDD) or phase field (PF) based models, have been employed to simulate the motion

of discrete dislocation in FCC crystals. These techniques access larger length and time scales than atomistic methods, but at the sacrifice of atomic-scale fidelity and requiring atomic scale input. With DDD, a suite of interactions, including cross slip, involving networks of several dislocations have been simulated [2, 38–43]. When cross slip is permitted, these studies have identified how changes in local stress state [39, 40, 42, 43] and the inclusion of locks and junctions [38–40] can affect material behavior. DDD relies on the line tension approximation to model dislocations as a series of connected nodes. The core structures of dislocations, such as an extended FCC core, are not directly predicted and dislocation movement and bypass maneuvers, such as cross slip, are governed *a priori* by a submodel, such as an Arrhenius law, e.g., [10]. Limited attention has been given to how intrinsic material properties affect cross slip [41]. PF-based models simulate dislocation motion from one state to another based on minimization of the system energy [44, 45]. These models can approximate the dislocation core structure while at the same time simulating the motion of long dislocations. Extended dislocations in FCC metals and alloys, as well as other crystal structures, like hexagonal close packed and $L2_1$ crystals, can be predicted when given stacking fault energy curves or surfaces from atomistic simulation [46–49]. Phase field dislocation codes have been employed to study, for a wide range of FCC metals, interactions of extended dislocations with each other, with voids, and with weak precipitates, wherein cross slip was not necessary [50–52]. Recently, a phase field dislocation method, a phase field microelasticity (PFM), was used to study the intersection outcomes of two opposite-signed screw dislocations gliding towards one another on different parallel planes in FCC Ir, Rh, and Cu [48]. In order to annihilate, the screw dislocations were permitted to move on a plane normal to the glide planes, which is not a cross slip plane. To date, cross slip in FCC metals has not been studied with phase field based techniques.

One phase field method, called phase field dislocation dynamics (PFDD), makes use of a regular computational grid as part of the fast Fourier transform solution procedure. Earlier versions of PFDD employed an orthogonal grid, which is appropriate when analyzing dislocation motion in a single slip plane or parallel planes. Recently, the PFDD

was extended to utilize non-orthogonal FCC or body center cubic (BCC) numerical grids [53]. In this way, grid points were aligned with crystallographic planes, which reduced error, minimized Gibbs oscillations, and enabled multiple non-parallel slip planes to be active. Using a BCC numerical grid, dislocation cross slip on crystallographic planes was demonstrated in Nb in PFDD [54]. In the model, cross slip was enabled because the screw dislocation cores are non-planar and compact. Because screw dislocations in FCC metals are planar and extended, the cross slip process in FCC metals differ from those of BCC metals.

In this work, we extend PFDD to permit cross slip by extended dislocations in FCC metals. The model is employed to simulate cross slip in eight pure FCC metals: Ag, Au, Cu, Ir, Ni, Pd, Pt, and Rh, under non-Schmid stress states or in the presence of a hard obstacle. All inputs are material properties obtained from either experiment, such as the anisotropic elasticity tensor, or DFT, for the full γ surface. With the same consistent method used for all material input, the PFDD simulations are designed to elucidate the material parameters that influence the propensity for cross slip. We find that the critical stress for cross slip is inversely proportional to the ratio of γ_{isf} to unstable stacking fault energy (γ_{usf}) and proportional to the equilibrium stacking fault width. Yet, there are usually one or two outliers metals in these relationships. We show that the cross slip stress, however, strongly scales with the anisotropic screw energy coefficient K_s without exception.

3 Methods

3.1 PFDD Overview

PFDD adopts the phase-field framework to simulate the motion of dislocations in a continuum. PFDD assigns an order parameter ϕ^α to the amount of slip on slip system α divided by the value of the Burgers vector $\mathbf{b}^\alpha$ on that system. A slip system is defined by the slip direction $\mathbf{s}^\alpha$ and plane normal vector $\mathbf{n}^\alpha$ [45]. For each slip system α, an order parameter integer value of $\phi^\alpha(\mathbf{x}) = n$ corresponds to a point $\mathbf{x}$ in three-dimensional space

being slipped by a dislocation n times, where n can be positive or negative depending on the sign of the dislocation. Interfaces between slipped and non-slipped regions are dislocation lines.

Given a configuration of dislocation lines, the increment in the configuration within a time increment is determined via the time-dependent Ginzburg-Landau equation (TDGL):

$$\frac{\partial \phi^{\alpha}(\mathbf{x})}{\partial t} = -m_0 \frac{\partial \Psi(\boldsymbol{\phi})}{\partial \phi^{\alpha}(\mathbf{x})} \tag{1}$$

where $\Psi(\boldsymbol{\phi})$ is the total free energy density and m_0 is the relaxation rate coefficient. The m_0 is non-negative and controls the rate of convergence to an equilibrium state. We find that a constant value of $m_0 \Delta t = 0.25\mu^{-1}$ or less, where μ is the effective isotropic shear modulus, ensures convergence in every time step for the entire time simulated. We note that under quasi-static loading, Equation 1 reduces to the minimization of the total free energy by the order parameters [55].

The $\Psi(\boldsymbol{\phi})$ is composed of three components:

$$\Psi(\boldsymbol{\phi}) = \psi_{ela}(\boldsymbol{\phi}) + \psi_{lat}(\boldsymbol{\phi}) - \psi_{ext}(\boldsymbol{\phi}) \tag{2}$$

The elastic energy $\psi_{ela}(\boldsymbol{\phi})$ is given by:

$$\psi_{ela}(\boldsymbol{\phi}) = \frac{1}{2} \int C_{ijkl} \epsilon^{e}_{ij}(\mathbf{x}) \epsilon^{e}_{kl}(\mathbf{x}) d^3x \tag{3}$$

where C_{ijkl} is the elastic stiffness tensor of the material and $\epsilon^{e}(\mathbf{x})$ is the elastic strain. The full anisotropic elastic C_{ijkl} is utilized in this work [56]. The total strain is the sum of $\epsilon(\mathbf{x}) = \epsilon^{e}(\mathbf{x}) + \epsilon^{p}(\mathbf{x})$, where $\epsilon^{p}(\mathbf{x})$ is the plastic eigenstrain due to the dislocations and is expressed as:

$$\epsilon^{p}(\mathbf{x}) = \frac{1}{2} \sum_{\alpha=1}^{N} \frac{b\phi^{\alpha}(\mathbf{x})}{d} \left(\mathbf{s}^{\alpha} \otimes \mathbf{n}^{\alpha} + \mathbf{n}^{\alpha} \otimes \mathbf{s}^{\alpha} \right) \tag{4}$$

where $\otimes$ is the tensor product operator, N is the number of slip systems, and d is the interplanar spacing.

The external energy $\psi_{ext}(\boldsymbol{\phi})$ represents the interaction between the dislocations and

the externally applied stress state:

$$\psi_{ext}(\boldsymbol{\phi}) = \int \sigma_{ij}^{app} \epsilon_{ij}^{p}(\mathbf{x}) d^3x \tag{5}$$

where σ_{ij}^{app} is the applied stress.

The lattice energy $\psi_{lat}(\boldsymbol{\phi})$ represents the energy penalty incurred when one crystalline half is displaced relative to the other half across the slip plane:

$$\psi_{lat}(\boldsymbol{\phi}) = \int \frac{\gamma_{sf}(\mathbf{x}, \boldsymbol{\phi})}{d} d^3x \tag{6}$$

where $\gamma_{sf}(\mathbf{x}, \boldsymbol{\phi})$ is the inelastic stacking fault energy surface. The $\gamma_{sf}(\mathbf{x}, \boldsymbol{\phi})$ involves displacements less than one lattice parameter, and it is common to use an atomistic calculation of the generalized stacking fault energy surface $\gamma_{gsf}(\mathbf{x})$ in its place. We find that the difference between the E^{isf} defined in [57] and the $\gamma_{gsf}(\mathbf{x})$ calculated from density functional theory (DFT) used here is zero at the maxima and minima and negligible elsewhere.

Finally we note that previous applications of PFDD for FCC materials included a gradient energy term ψ_{gra} in the total free energy in Eq. 2 [50]. The effect of ψ_{gra} and variations in the gradient energy coefficients were systematically studied in [46]. It was found that the coefficients primarily affect the widths of the partial dislocation cores and only led to second-order effects on the equilibrium stacking fault widths (SFW) and widths of the individual Shockley partial dislocations. Additionally, the gradient energy coefficients can be adjusted to align core structures with those from MS simulations [50]. However, MS models need reliable interatomic potentials, which not all metals considered in our study have. For these reasons, in this work ψ_{gra} is omitted.

3.2 Modeling extended FCC dislocations

In the present application, order parameters correspond to $\langle 110 \rangle \{111\}$ slip systems. While all 12 $\langle 110 \rangle \{111\}$ slip systems can be included in simulation, we consider only the three slip systems on the habit plane and the three slip systems on the cross slip

$(\bar{1}\bar{1}1)$ plane. These six order parameters are listed in 1. Order parameters can alternatively be assigned to the two independent directions within the {111} plane. Either choice for the order parameter set does not change the results.

The motion of an extended dislocation is tracked by its disregistry ζ^β, which is given by [46]:

$$\zeta^\beta(\mathbf{x}) = \sum_{\alpha=1}^{n_{sp}} \phi^\alpha(\mathbf{x}) \mathbf{b}^\alpha \cdot \mathbf{s}^\beta \tag{7}$$

where n_{sp} is the number of order parameters lying on a slip plane, $\mathbf{b}^\alpha$ is the Burgers vector corresponding to the αth order parameter and $\mathbf{s}^\beta$ is the slip vector component in the βth direction. With three slip systems per {111} type plane, $n_{sp} = 3$. Order parameters need only have non-zero values on the active glide planes and therefore the evolution of each order parameter is confined to its corresponding slip plane.

Order parameter	Burgers vector	Slip plane normal
ϕ^1	$[\bar{1}10]$	(111)
ϕ^2	$[10\bar{1}]$	(111)
ϕ^3	$[0\bar{1}1]$	(111)
ϕ^4	$[\bar{1}10]$	$(\bar{1}\bar{1}1)$
ϕ^5	$[101]$	$(\bar{1}\bar{1}1)$
ϕ^6	$[0\bar{1}\bar{1}]$	$(\bar{1}\bar{1}1)$

Table 1: Six order parameters used in the FCC PFDD simulations.

3.3 Material Parameters

The formulation is applied to eight pure FCC metals. For input into the model, we use lattice parameters and elastic constants from experimental measurements at room temperature [58] and γ-surfaces from DFT [59]. Table 2 lists their values. For reference, the Zener ratio is a term commonly used to quantify elastic anisotropy in cubic materials, defined as $\frac{2C_{44}}{C_{11}-C_{12}}$. A Zener ratio of 1 corresponds to an isotropic material. The local minimum γ_{isf} and unstable stacking fault energy (γ_{usf}) are taken from the γ-line along the $\langle 112 \rangle$ direction. A wide range of γ_{isf} and γ_{usf} are covered by these eight metals,

making this set appropriate for probing material influences on cross slip propensities. Furthermore, in comparing their Zener ratios, we observe that these eight metals also differ widely in their degree of elastic anisotropy.

The differences in elastic constants from DFT and the experimental measurements are minor except for Au. The significant difference between them has been shown previously to affect the predictions on dislocation behavior for twinning in Au [60]. For Au only, we repeat calculations using the DFT calculated moduli, labeled Au_1. The other set using experimental values is marked as Au_2.

Material	b (nm)	C_{11} (GPa)	C_{12} (GPa)	C_{44} (GPa)	Zener Ratio	γ_{isf} (mJ/m^2)	γ_{usf}(mJ/m^2)
Ag	0.289	122	92	45.5	3.03	14.49	92.01
Au_1	0.294	152	134	27.7	3.11	26.79	76.68
Au_2	0.288	191	162	42.2	2.91	26.79	76.68
Cu	0.256	176	129	75.2	3.19	41.83	160.5
Ir	0.271	580	242	256	1.51	385.9	671.7
Ni	0.249	247	153	122.0	2.60	152.1	300.9
Pd	0.275	221	171	70.8	2.83	135.5	214.9
Pt	0.277	347	251	76.5	1.59	280.9	297.9
Rh	0.269	413	194	184	1.68	208.7	475.3

Table 2: FCC elements studied here and their material properties [58, 59]. For Au, the DFT-calculated elastic constants are denoted as Au_1 and the experimentally measured ones are Au_2.

3.4 Incorporating DFT-calculated γ-surfaces

For $\gamma_{gsf}(\mathbf{x})$ in ψ_{lat}, the entire γ-surface is used as input. The γ-surface for all eight FCC metals have been calculated previously by DFT [59] and each is represented by a fine grid of 64 x 100 points. Although sufficiently fine to access in calculation as a look-up table, for numerical stability, it is desirable to parameterize the surface by a smooth function. Schoeck had presented a parameterization using only seven points, which has been widely used in phase field dislocation codes [46, 47, 61, 62]. However, due to deviations in surface topology from the ideal FCC bond structure, many features of the actual γ-surface are missed. Later a function utilizing 11 points was proposed that

improved the representation and provided more accurate predictions of core structures from PFDD compared to those using the original Schoeck function [50, 56]. Yet differences in prediction still persist compared to using a look-up table for the full γ-surface. In the present calculations, we employ the CASM package MultiShifter [63] to produce a function that provides a high-fidelity representation of the γ-surfaces from Su et al. [59]. For all eight metals, the γ-surface follows a trigonometric series, given by

$$\begin{aligned}\gamma_{gsf}(\Delta_{110}, \Delta_{112}) = &\sum_n \sum_m A_{nm} \cos\left(\frac{2\sqrt{2}\pi n \Delta_{110}}{a_0} + \frac{2\sqrt{2}\pi m \Delta_{112}}{\sqrt{3}a_0}\right) \\ &+ \sum_o \sum_p B_{op} \sin\left(\frac{2\sqrt{2}\pi o \Delta_{110}}{a_0} + \frac{2\sqrt{2}\pi p \Delta_{112}}{\sqrt{3}a_0}\right)\end{aligned} \tag{8}$$

where a_0 is the material lattice parameter and Δ_{hkl} refers to displacement of the crystal along the $[hkl]$ direction on the $\{111\}$ plane. To prevent overfitting, terms with $A_{nm} < 1.0$ or $B_{op} < 1.0$ are omitted. The final number of terms varied from 28 to 38 depending on the metal. The coefficients are listed in Appendix 8.1. As an example of the level of accuracy achieved, for Cu, Ni, and Pt, Figure 1 compares the DFT calculated points with the function along the $[\bar{1}10]$ and $[1\bar{2}1]$ directions, which is the likely path taken by the dislocations. The topology of the surfaces are fully captured.

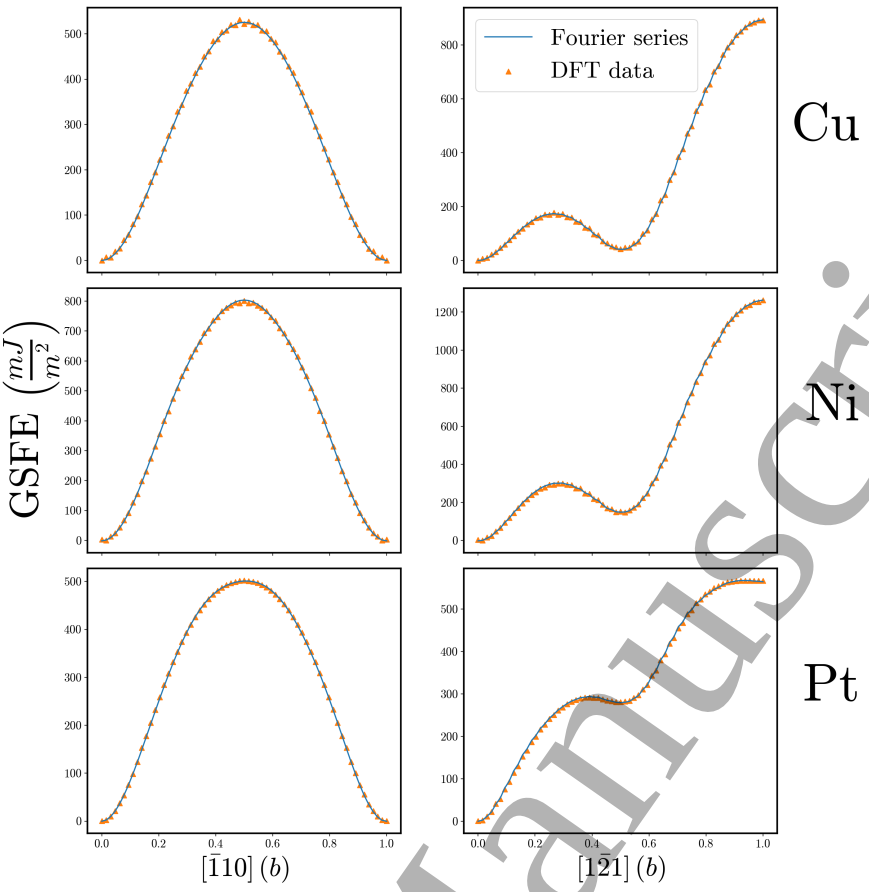

Figure 1: Comparison of the generalized stacking fault energy curves for Cu, Ni, and Pt along the $[\bar{1}10]$ and $[1\bar{2}1]$ directions, between the DFT calculated points from the γ-surface [59] and the parameterized function derived using MultiShifter [63]

.

Finally, the γ_{gsf} is expressed in terms of the three order parameters. When the derivatives are taken with respect to the order parameter in Eq. (1), they are related via:

$$\frac{\partial \gamma_{gsf}}{\partial \phi^1} = \frac{\partial \gamma_{gsf}}{\partial \Delta_{110}} \tag{9}$$

$$\frac{\partial \gamma_{gsf}}{\partial \phi^2} = -\frac{1}{2}\frac{\partial \gamma_{gsf}}{\partial \Delta_{110}} + \frac{1}{2}\frac{\partial \gamma_{gsf}}{\partial \Delta_{112}} \tag{10}$$

$$\frac{\partial \gamma_{gsf}}{\partial \phi^3} = -\frac{1}{2}\frac{\partial \gamma_{gsf}}{\partial \Delta_{110}} - \frac{1}{2}\frac{\partial \gamma_{gsf}}{\partial \Delta_{112}} \tag{11}$$

The present work is the first application of the PFDD method with an FCC non-orthogonal grid and high fidelity parameterization of the full DFT γ-surfaces.

3.5 Simulation set-up

Figure 2 shows the simulation cell containing an initial screw dipole. The simulation cell is created with primitive vectors $p_1 = [\bar{1}0\bar{1}]\,, p_2 = [\bar{1}10]\,, p_3 = [01\bar{1}]$. The primitive vectors of the discretized crystal are equivalent to the primitive FCC vectors, and the distance between neighboring discrete grid points is equal to $1b$.

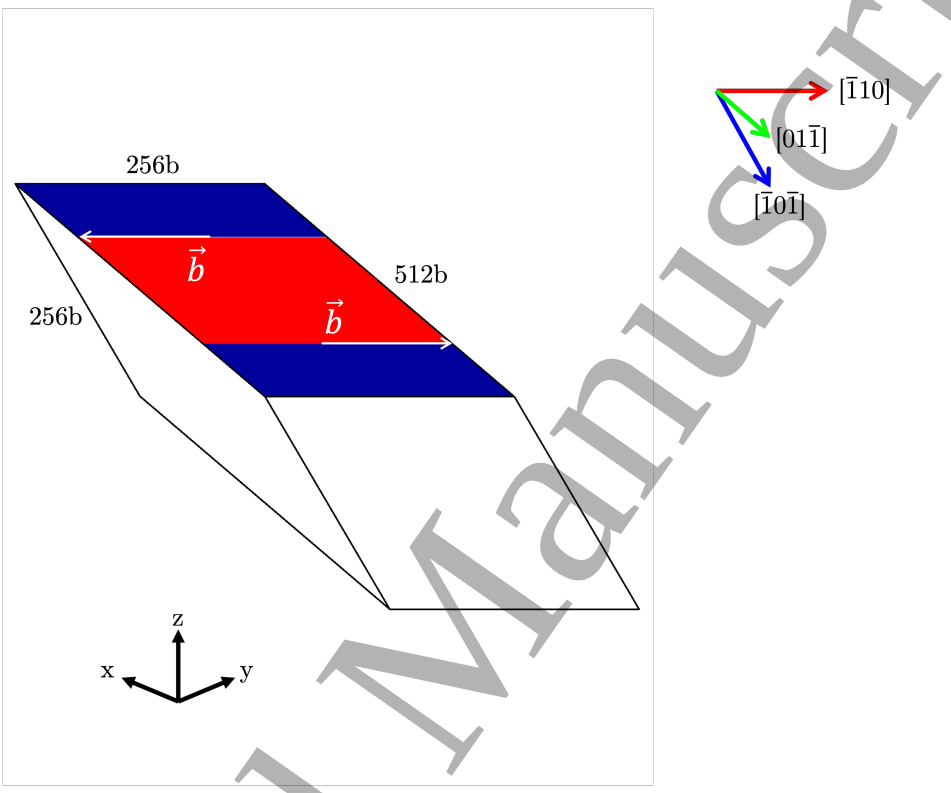

Figure 2: Schematic of the simulation cell containing a screw dislocation dipole. To show the non-orthogonality of the grid, the view direction is $[33\bar{2}]$.The underlying computational grid is FCC and the edges of the cell correspond to the primitive vectors indicated by the colored coordinate system. The Cartesian coordinate system is given on the bottom left. The dislocation is the interface between the slipped domain (red) and outer unslipped region (blue). The screw dislocation Burgers vector are indicated.

Figure 3 shows the model set up used for all simulations. A screw dislocation dipole of $\left(\mathbf{b} = \frac{a}{2}\,[\bar{1}10]\right)$ with a spacing of $256b$ is initialized by setting $\phi^1 = 1$ along the middle half of the topmost (111) plane. The spacing used is sufficiently wide such that dipole does not self annihilate under zero stress. The simulation cell dimensions are $256b \times 256b \times 512b$. The cell size and dipole length are determined to ensure the effect of periodic boundary conditions on the properties and dynamic behavior of the dislocations are negligible. We define a suitable simulation cell size at the point where the equilibrium SFW maintains

a constant value. Smaller dipole spacings and simulation cell sizes were found to be insufficient to properly simulate dislocation behavior in all studied materials without the dislocation being affected by the stress field of its periodic image. All simulations that follow are performed until convergence, where the global Euclidean norm of the order parameter fields is less than a tolerance value of 0.0001. Lowering it further to 10^{-8} changes results by less than 0.006%.

When the system is relaxed under zero stress, the initially compact dislocations each dissociate into two equal partials, which move apart to an equilibrium distance, forming a stacking fault in between. We confirm that these partials have an $\frac{a}{6}\langle 112\rangle$-type Burgers vector. From the relaxed configuration, the disregistry field for each partial is calculated by projecting the disregistry parallel and perpendicular to the slip direction along each partial direction. In this way, the locations of both partials can be identified and their distance, the stacking fault width (SFW), calculated.

Once the equilibrium core structure is achieved, a far field stress is applied to determine the minimum stress to move the dislocation in an obstacle free crystal. The applied stress tensor produces a shear resolved parallel to the glide plane and in the direction of the Burgers vector. The magnitude of shear is increased by 0.0001μ until both the leading and trailing partial have moved a distance $1b$. We denote the corresponding threshold value by τ^0. We use the τ^0 values for the eight metals as a reference to compare with the critical stress for cross slip and facilitate comparisons among the metals. (The τ^0 could also be called a lattice friction stress or Peierls stress, although τ^0 is not expected to compare with Peierls stress values from *ab initio* or atomistic simulations.)

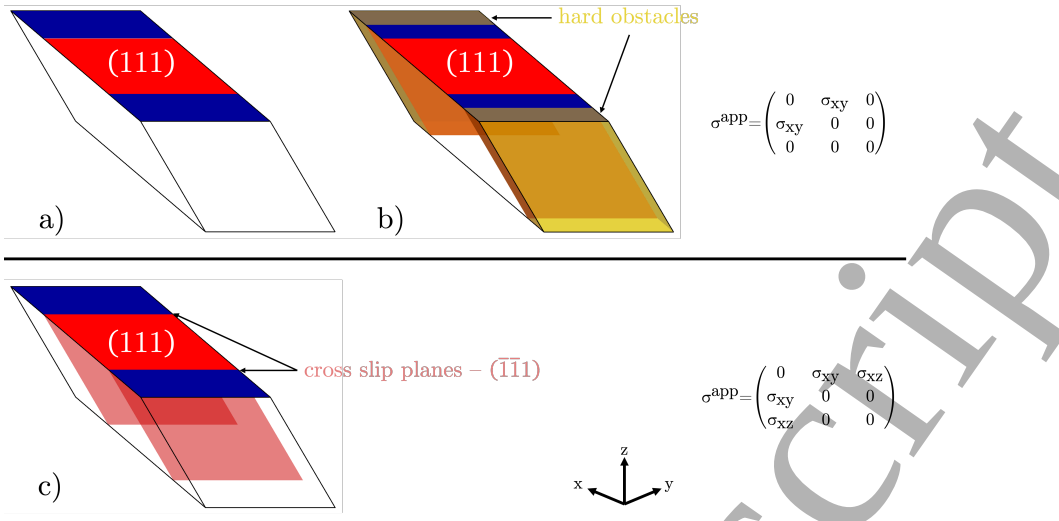

Figure 3: Simulation set-up for calculation of a) τ^0, b) τ^0_{CS}, c) τ_{CS}. To show the non-orthogonality of the grid, the view direction is $[33\bar{2}]$. On the right of each set up, the applied stress tensor is given. Only the non-zero stress components in Cartesian coordinates are shown. The cross slip planes are highlighted in light red, and obstacles are in yellow.

We also use the same set up to determine a critical stress for cross slip. The stress tensor shown in 3b is applied to the crystal containing the dislocation dipole initially on the habit plane (see 3a. This stress state is a type of "non-Schmid" stress. The resolved shear stress on the habit plane is zero and the resolved shear stress on the cross slip plane is non-zero. The norm of the applied stress is increased in increments of 0.001μ until both partials transition from the habit to the cross slip plane. The threshold stress for this event is denoted by τ^0_{CS}. It corresponds to the minimum stress needed to transfer a full screw dislocation from one plane to another without the involvement of an obstacle. In determining τ^0_{CS} for all metals, the ratio of the shear components in the applied tensor is kept the same.

In the conventional picture of cross slip, a dislocation glides in its habit plane under an applied stress, intersects an obstacle, and attempts to bypass it by cross slip. Obstacles, such as precipitates or other dislocations (glissile or sessile), can produce a stress field of their own, which can interact with the approaching dislocation. In this work, we aim to promote cross slip without the effect of the stress field produced by the defect. Accordingly, in the final set of simulations, we demonstrate dislocation cross slip when interacting with a strong coherent obstacle. The obstacle bears the same elastic properties

as the metal and has a lattice energy calculated from the metal γ-surface, but in this region the values of the γ-surface are multiplied by a scaling factor of 2.25. This magnification is sufficiently high to incite cross slip rather than obstacle shearing for all eight metals and does not generate an elastic field. Obstacles of size $256b \times 256b \times 64b$ are inserted near each edge of the simulation cell as shown in Figure 3c. Since the aim is to demonstrate cross slip, we elect to apply a stress state that imposes equal resolved shear stresses on the habit and cross slip planes [54]. The norm of the tensor is increased in increments of 0.001μ until both leading and trailing partials cross slip onto the cross slip plane. For the sake of comparison among the eight metals, the minimum stress for this event is indicated by τ_{CS}.

4 Results

4.1 Equilibrium core structure and stacking fault widths (SFW)

We first examine the stress free, equilibrium core structures of the screw dislocations in all eight metals. As mentioned, in every metal examined, the initial compact screw dislocation dissociates into two Shockley partials with a stacking fault in between after relaxing the system. Table 3 lists the equilibrium SFWs in terms of b. Pt has the narrowest core at $0.62b$ and Ag the widest at $4.58b$. Compared to prior work utilizing PFDD [50, 56], the values from the present work are either similar or lower in value. Any differences could arise from the fact that here, the grid points coincide with FCC lattice points and the γ-surface is an accurately parametrized smooth function. With the FCC grid, the density of grid points is equal on all slip planes, providing a more accurate solution [53].

The SFWs result from a balance between the repulsive elastic interaction energy between the partials and energy penalty in the stacking fault their separation creates. A higher shear modulus will tend to widen the stacking fault by increasing the repulsive elastic energy, while a higher γ_{isf} will tend to shorten the stacking fault by increasing the energy required for partial dissociation. As anticipated, the PFDD SFWs in Table 3

Material	$SFW^{aniso}\,(b)$	$SFW^{iso}\,(b)$
Ag	4.58	13.26
Au_1	1.89	3.65
Au_2	3.29	6.48
Cu	1.53	6.17
Ir	1.90	3.02
Ni	1.28	2.75
Pd	1.07	2.15
Pt	0.62	0.88
Rh	2.68	3.92

Table 3: Equilibrium SFWs for screw dislocations calculated using PFDD for eight FCC elements, normalized by their Burgers vector. Au_1 denotes SFW calculated using DFT-calculated elastic constants [59] and Au_2 using experimental elastic constants [58].

increase with shear modulus and decrease with γ_{isf}.

Based on the energy balance, dislocation theory provides an expression for the separation between two already separated Shockley partials. The theory has long given the expectation that SFWs should increase with stiffness and Burgers vector size and decrease with γ_{isf}. When assuming isotropic elasticity, the analytical separation for any character dislocation is [1]:

$$SFW^{iso}_{analytical} = \frac{\mu}{2\pi\gamma_{isf}}\left[(\boldsymbol{b_L}\cdot\boldsymbol{\xi_L})(\boldsymbol{b_T}\cdot\boldsymbol{\xi_T}) + \frac{(\boldsymbol{b_L}\times\boldsymbol{\xi_L})\cdot(\boldsymbol{b_T}\times\boldsymbol{\xi_L})}{1-\nu}\right] \tag{12}$$

and when considering anisotropic elasticity, it is

$$SFW^{aniso}_{analytical} = \frac{b^2}{8\pi\gamma_{isf}}\left(K_s - \frac{1}{3}K_e\right) \tag{13}$$

For a screw dislocation, $\boldsymbol{b_L} = \frac{a}{6}[\bar{2}11]$, $\boldsymbol{b_T} = \frac{a}{6}[\bar{1}2\bar{1}]$, and $\boldsymbol{\xi_L} = \boldsymbol{\xi_T} = \frac{1}{\sqrt{2}}[\bar{1}10]$. In Eq. 13, K_s and K_e are the screw and edge energy coefficients dependent on the elastic constants [1]:

$$K_s = \sqrt{\frac{C_{44}\left(C_{11}-C_{12}\right)}{2}} \tag{14}$$

$$K_e = \frac{1}{3}\left(\overline{C}'_{11}+C_{12}\right)\left(2+\frac{C_{11}+\frac{H}{2}}{\overline{C}'_{11}}\right)\sqrt{\frac{C_{44}\left(\overline{C}'_{11}-C_{12}\right)}{\left(\overline{C}'_{11}+C_{12}+2C_{44}\right)\left(C_{11}+\frac{H}{2}\right)}} \tag{15}$$

where $H = 2C_{44} + C_{12} - C_{11}$ and $\overline{C}'_{11} = \sqrt{C_{11}\left(C_{11} + \frac{H}{2}\right)}$. In this work, the elastic constants were selected from room temperature experimental data [58] and DFT calculations [59].

For reference, the PFDD SFWs are compared to the isotropic and anisotropic elasticity model. To enable comparisons with the former, the PFDD calculations are repeated using an equivalent isotropic elasticity tensor in place of the full anisotropic one for each metal. Plots comparing PFDD with these analytical models are provided in the Appendix 8.2. The analytical model agrees very well with the PFDD SFWs in the isotropic case. This nearly perfect agreement between the isotropic SFWs across several FCC metals was not achieved with prior PFDD studies.

The analytical model, however, consistently overestimates the PFDD SFWs in the anisotropic case. In its derivation, the analytical model does not account for features of extended core, such as the finite core width of the partials and inhomogeneous displacements across the fault width present in the calculated core structure. The energetic penalty is only associated with the local minimum in the γ-surface. The deviations from the PFDD SFWs are largest for Cu and Ag, the most anisotropic metals considered here. The comparison with PFDD SFWs implies that many of these features in γ-surface are important in determining the SFWs when elastic anisotropy is considered.

To elucidate the role of elastic anisotropy, Figure 4 shows the ratio of the anisotropic SFW to the isotropic one calculated from PFDD vs. Zener ratio. For a screw dislocation, the effect of elastic anisotropy is to reduce the SFW. As the degree of anisotropy increases, the more the SFW reduces relative to the isotropic case. Anisotropy results in interactions between screw and edge segments, which are not present under the assumption of ideal elastic isotropy. As the level of anisotropy increases, the screw/edge interactions weaken the repulsive interaction between the two partials, drawing the partials closer, than with anisotropy removed. This trend is predicted by the analytical model as well as by another analytical model extended to account for finite partial core widths [64].

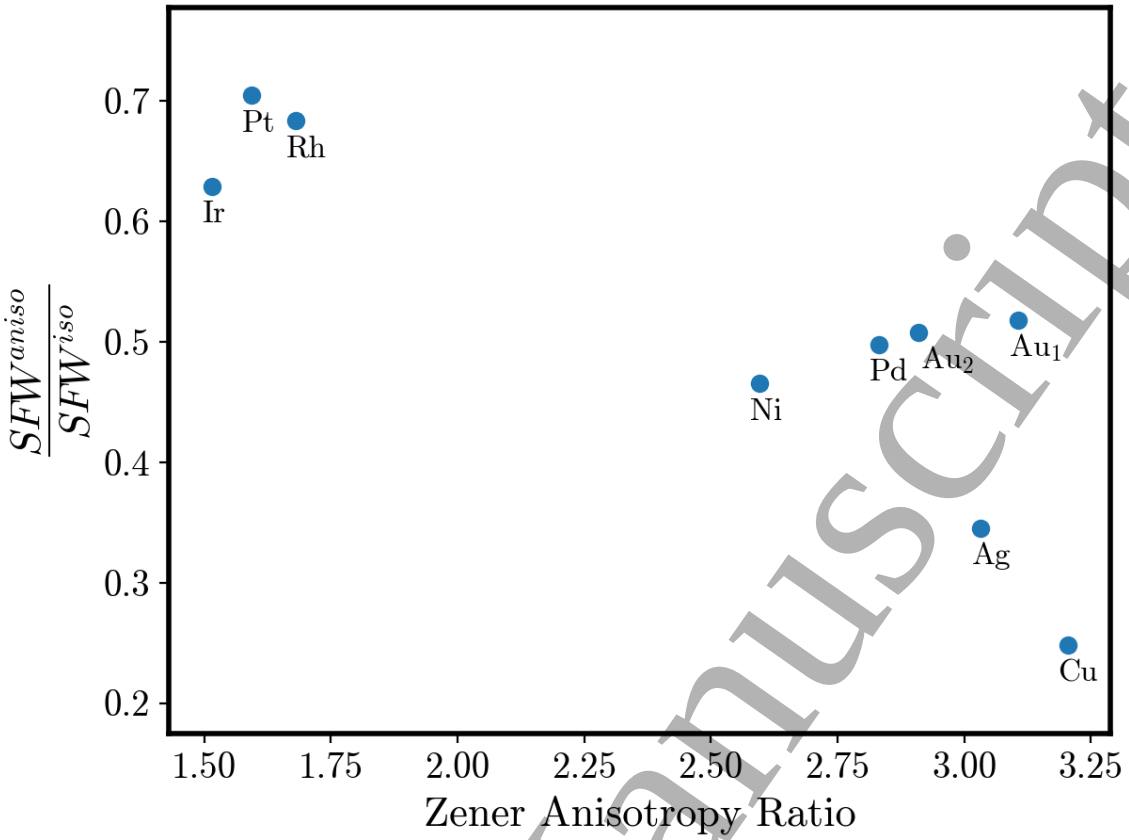

Figure 4: Ratio of the anisotropic SFW to isotropic SFW as calculated by PFDD for eight FCC metals versus their Zener ratio.

Next we study the σ_{xz} and σ_{yz} stress fields generated by the screw dislocations. Figure 5 presents the fields for Cu with a moderately spread core and Pt, with the narrowest core. The fields are asymmetric about both the x and y directions. The asymmetry results from elastic anisotropy, wherein the degree of asymmetry scales with the degree of anisotropy, being greater in Cu than in Pt. The minor fluctuations seen in the fields are due to Gibbs oscillations. These variations arise from difficulties in representing the discrete strain in Fourier space. Using the non-orthogonal grid has minimized these such that they are not large compared to the value of the stresses [53].

For comparison, the stress fields generated by PFDD for Pt when assuming elastic isotropy and the analytical prediction from dislocation theory for these stress fields for a perfect dislocation in an isotropic material is provided in Figures 6b and 6c, respectively. We show the isotropic analytical solution to provide verification for PFDD to produce

continuum dislocation stress fields. This isotropic solution is well-known [1], while the analytical anisotropic elastic solution is numerical and less familiar. We also highlight and isolate the role of elastic anisotropy in Figure 6 via a comparison of the PFDD-generated isotropic and anisotropic elastic stress fields. Direct comparisons with this analytical field shows that the asymmetry in the PFDD fields in Figure 5 results from elastic anisotropy. The intensity of the fields is reduced, more so for the wider core in Cu than Pt. The comparison with the analytical result also highlights the influence on the extended core on the stress field. Stress fields formed by perfect screw dislocations in BCC metals as simulated by PFDD were previously found to closely approximate the analytical solution for the stress field of a single perfect screw dislocation [54]. For BCC metals, the core is compact and symmetrically extended. For FCC metals, however, the planar dissociation causes the stress fields to diverge from the analytical fields. For the dissociated core, the stress field spreads in plane and maximum intensity regions surround the two partials. For Cu, a material with the larger SFW, the σ_{yz} stress field changes sign between the Shockley partials. Even in the case of Pt, with the narrowest core and under the assumption of isotropic elasticity as shown in Figure 6b, the dissociated core produces a stress field that deviates from the analytical field.

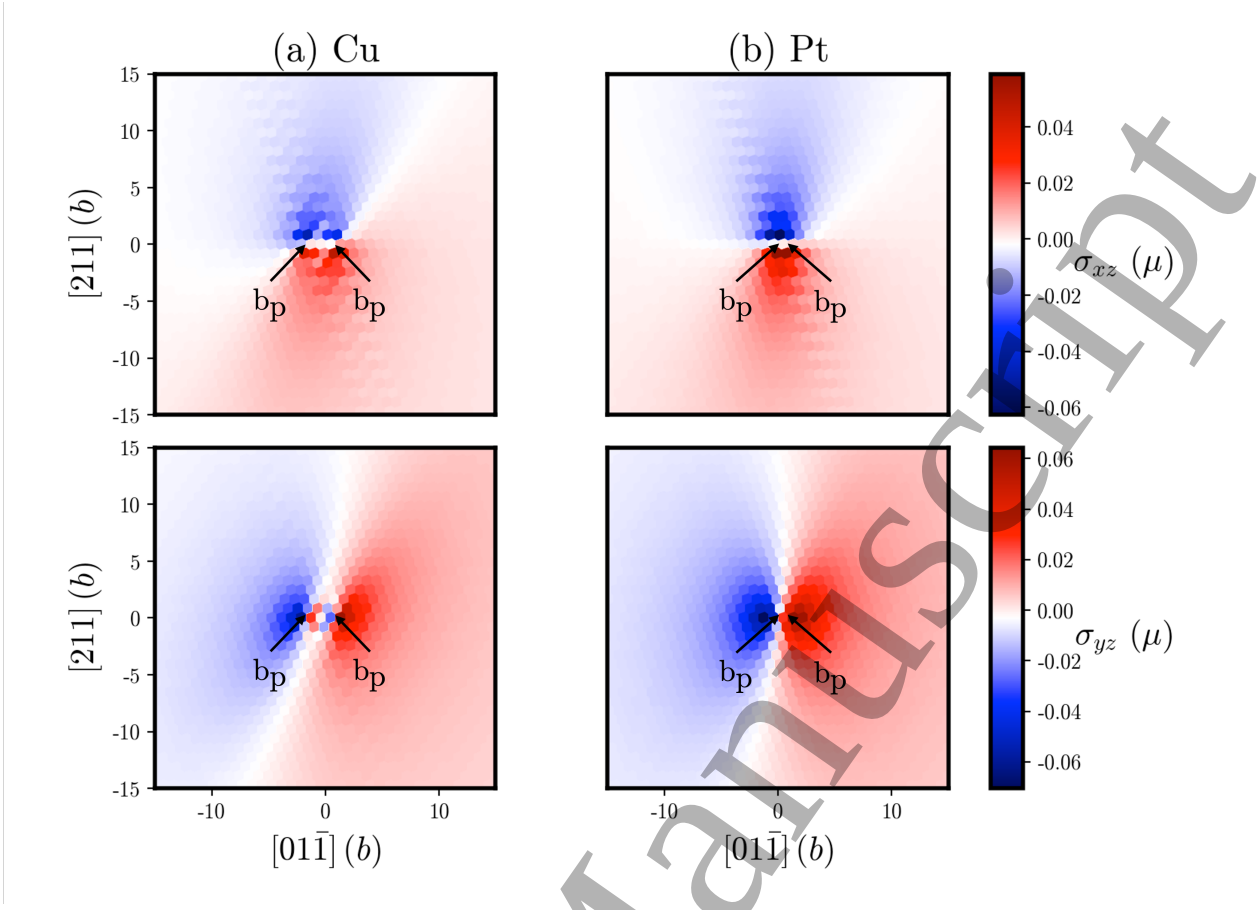

Figure 5: Anisotropic elastic stress fields generated by an extended screw dislocation in (a) Cu and (b) Pt as calculated by PFDD. Locations of the Shockley partials are indicated.

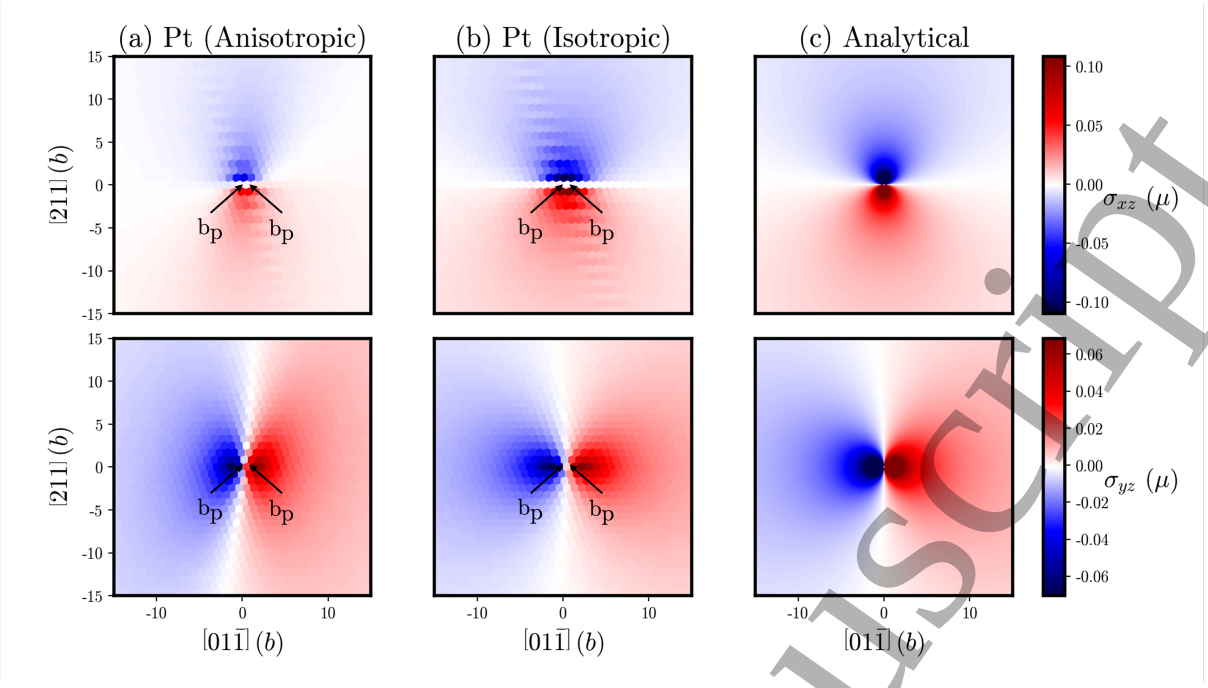

Figure 6: The out of plane shear stress fields for an extended screw dislocation in Pt as calculated by PFDD when assuming (a) elastic anisotropy and (b) elastic isotropy. Locations of the Shockley partials are indicated. (c) The analytical isotropic elastic solution.

4.2 Dislocation cross slip

The response of the dislocation to the non-Schmid stress was simulated for all eight metals. The screw dislocations cross slip when given sufficient amount of stress, at or above a τ^0_{CS}, in all metals except Ag. Figure 7 shows the time progression of cross slip using the dislocation disregistry for Ni. At zero stress the dislocation is extended on the (111) habit plane. At a threshold value τ^0_{CS}, the dislocation first constricts over the entire line length, and the compact dislocation cross slips onto the $(\bar{1}\bar{1}1)$. The observed process of both Shockley partials constricting and transferring to the $(\bar{1}\bar{1}1)$ plane corresponds to the Friedel-Escaig mechanism [24, 28]. We note that their model proposes that the dislocation constricts over a segment of the line, followed by it bowing out onto the cross-slip plane. In agreement, PFDD predicts that the dislocation constricts on the glide plane before cross slipping onto the cross-slip plane. Because we do not include thermal fluctuations, the dislocation line constricts uniformly along its length.

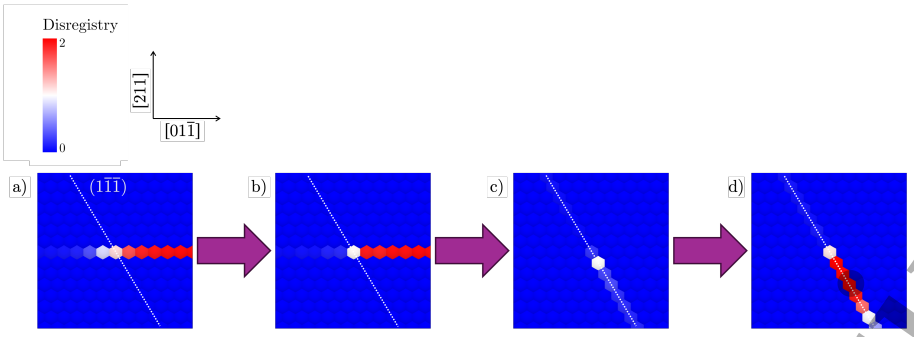

Figure 7: Snapshots showing a Ni screw dislocation on the $(1\bar{1}\bar{1})$ plane (denoted by a dashed white line) at (a) under zero applied stress. When the stress rises above the threshold cross slip stress, the screw dislocation (b) constricts and (c-d) glides on the cross slip plane. The disregistry is shown to indicate location of the dislocations.

Next, under a mixed stress state, the dislocation is driven towards an obstacle. Using Ni and Ag as examples, Figure 8 shows the time evolution of a screw dislocation. The moving dislocation intersects the obstacle, constricts and then cross slips onto the cross slip plane. All metals cross slip again via the Friedel-Escaig mechanism, upon intersecting the obstacle, differing only in the τ_{CS} needed.

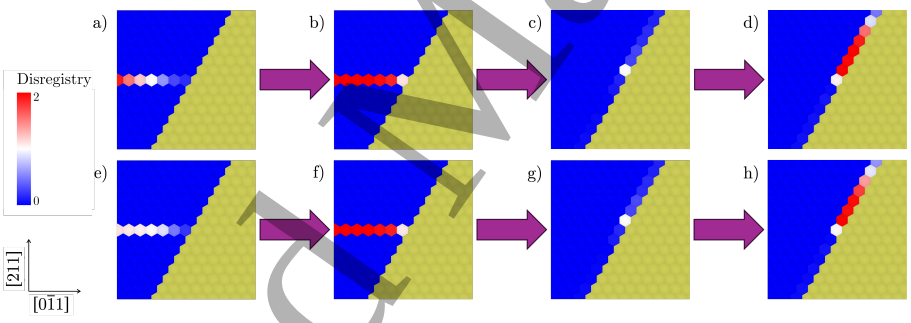

Figure 8: Snapshots showing time evolution in glide of a screw dislocation in (a)-(d) Ni and (e)-(h) Ag on the $(1\bar{1}\bar{1})$ under an applied stress. (a),(e) approaching the obstacle, (b),(f) constriction at the intersection with the obstacle and (c-d),(g-h) cross slip. The disregistry is shown to indicate location of the dislocations. The obstacle is in yellow.

5 Discussion

5.1 Critical stresses

We take advantage the full suite of metals to compare their propensities for cross slip. We first consider the role of material yield strength, with the expectation that the greater the stress to move dislocations, the more difficult it could be to cross slip as well. Figure

9a contrasts τ^0 and cross slip τ^0_{CS}, when both are normalized by K_s. The normalization by stiffness is made in efforts to facilitate their comparison by removing fundamental differences in bond strength and stress levels they would experience at yield. Figure 9a shows that τ^0 is approximately an order of magnitude lower than τ^0_{CS}. We also see that with the exception of Rh, the harder it is for the dislocation to glide, the harder too it is to cross slip. Relative to its stiffness, Rh has an unusually high τ^0_{CS} and cross slip would not be expected.

Dislocation behavior in PFDD is influenced by the entire γ-surface not only the local minimum γ_{isf}. The key energetic points along the pathway taken by the Shockley partial dislocations are γ_{isf} and γ_{usf}. To study their influence on cross slip, Figure 9b probes the effect of the ratio $\gamma_{isf}/\gamma_{usf}$ on the normalized τ^0_{CS}. With exception of Pt, τ^0_{CS} decreases as $\gamma_{isf}/\gamma_{usf}$ increases. The implication from this observation is that more than γ_{isf} can influence cross slip propensities. This finding is in agreement with some experimental mechanical tests on pure Ag, Au, Cu, and Ni [65, 66]. As seen in simulation, a key step in the cross slip process is core constriction prior to transfer to the cross slip plane. Less resistance to constriction is afforded by high γ_{isf} and low γ_{usf}. In the case of Pt, γ_{isf} and low γ_{usf} are known to be exceptionally close. Unlike the other FCC metals, the intrinsic stacking fault in Pt is associated with a shallow well in the energetic landscape. The screw dislocation in Pt core lacks the distinctive structure expected of FCC metals. The boundaries between the partial and stacking fault within the core are diffuse.

As constriction is seen here in simulation to be a necessary step for cross slip, τ^0_{CS} is expected to scale with SFW. Materials with larger equilibrium SFWs are anticipated to require more energy to overcome the repulsive force between Shockley partials and constrict [25, 64]. Figure 9c plots τ^0_{CS} against SFW. Neither quantity is normalized in this case so that the cross slip tendencies of these metals can be directly compared. As expected τ^0_{CS} increases with SFW. An unexpected exception, however, is seen for Au. Au has an unusual ease for cross slip despite its large SFW. It is worth noting that an outstanding feature of Au is its very low shear modulus.

The compliant Au as an outlier in Figure 9c points to a possible influence of K_s.

Further, the relationships seen in Figure 9a,b are not notably strong and in both, K_s is used in normalization. Figure 9d examines the impact of K_s on cross slip. As shown, τ_{CS}^0 strongly correlates with K_s. The two stiffest materials Rh and Ir have the highest τ_{CS}^0 and the most compliant Au the lowest. The substantial influence of K_s explains some of the exceptions seen with respect to the properties in Figure 9a-c. The large shear compliance of Au and the large shear stiffness of Rh play an even greater role in their cross slip propensity than first thought. Additionally, our finding that K_s influences cross slip more strongly compared to γ_{isf} and the SFW is contrary to traditional analytical models of the Friedel-Escaig mechanism, which place more emphasis on the latter two parameters to dominate the constriction and cross slip process [13, 67].

The profound effect of K_s seen in Figure 9d should prevail in other cross slip situations. Figure 10 plots the minimum stress τ_{CS} calculated for a screw dislocation to naturally cross slip when faced with a hard obstacle and mixed stress state. As shown, τ_{CS} directly scales with K_s. Again, it is found that shear stiffness strongly influences cross slip. The results contrast traditional analytical models of the Friedel-Escaig mechanism, which place more emphasis on γ_{isf} or SFW to dominate the constriction and cross slip process [13, 26]. The work of Saada is particularly applicable to our own. An analytical line tension model was developed to capture the activation energy for cross slip where both Shockley partials constrict and re-emerge on the new slip plane in the same direction relative to the original dislocation, which is what we observe in PFDD. A formula for the constriction energy accounting for anisotropic elasticity was derived and was found to vary roughly equally with both γ_{isf} and the SFW [13]. Thus, while our expectation based on analytical models is that these two parameters would show a dominant relationship with τ_{CS}^0 or τ_{CS}, it is in fact the anisotropic screw energy coefficient that agrees better with the critical cross slip stress. The present approach is unique in that the roles of these properties are studied by preserving holistically all the properties of these metals (i.e., anisotropic stiffness, lattice parameter, γ-surface) rather than hypothetically isolating only one property and that a large suite of FCC metals are simulated using the same methodology. Further experimental characterization is needed to validate the relative

propensities of cross slip among these metals.

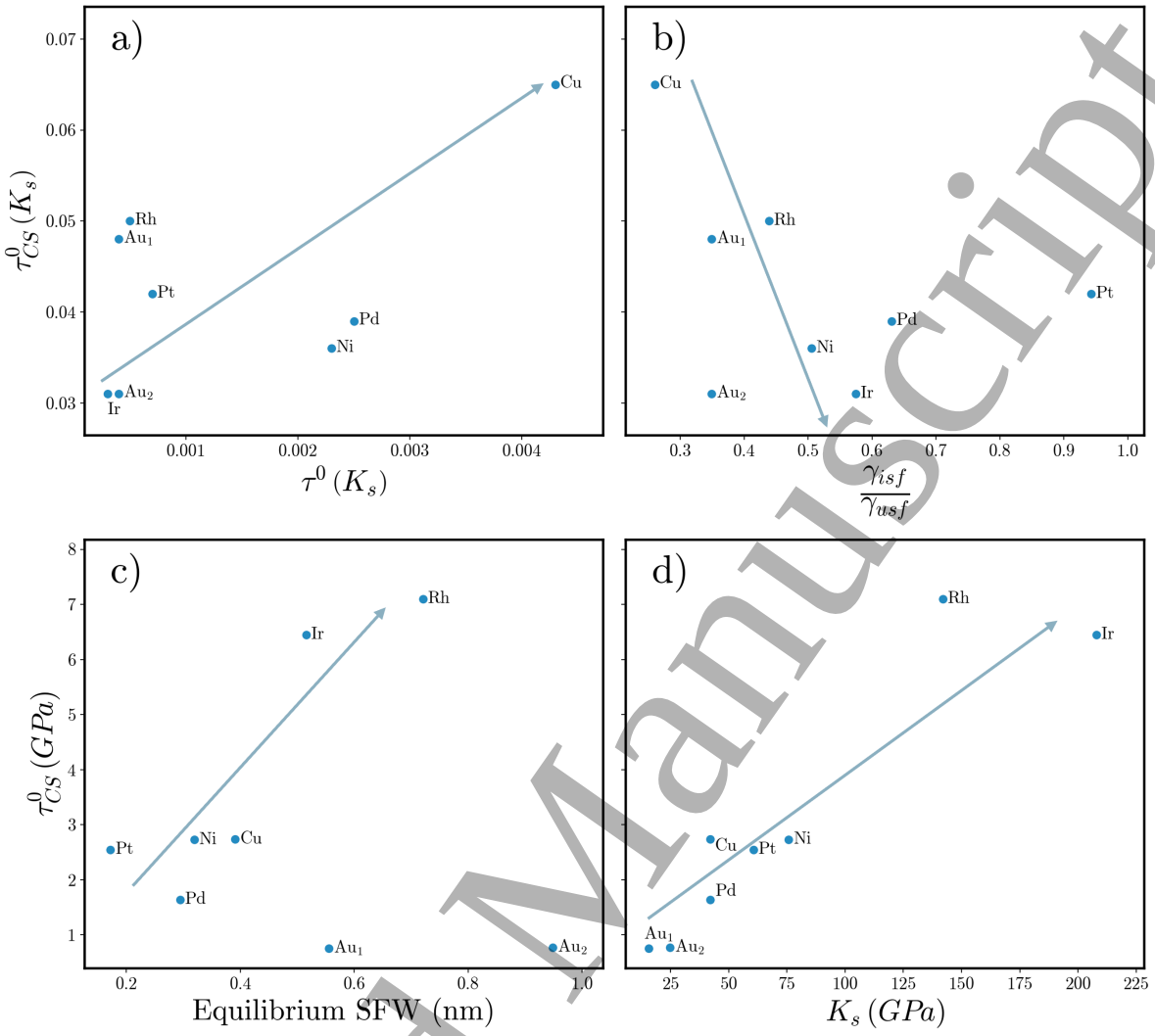

Figure 9: a) τ^0_{CS} plotted as a function of τ^0. Both stresses are normalized by the anisotropic screw energy coefficient K_s, b) τ^0_{CS} normalized by K_s versus $\gamma_{isf}/\gamma_{usf}$ ratio. c) τ^0_{CS} as a function of calculated equilibrium SFW, and (d) τ^0_{CS} as a function of K_s.

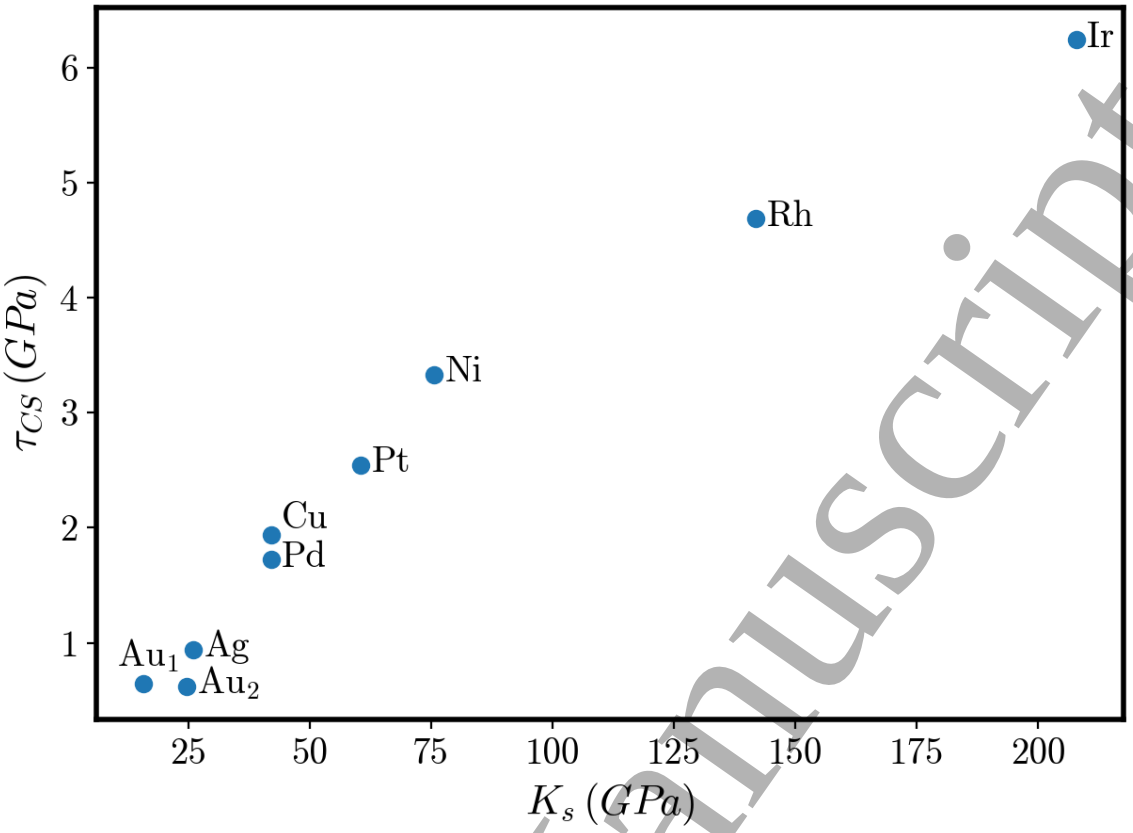

Figure 10: τ_{CS} versus anisotropic screw energy coefficient K_s.

While we design our simulations to observe cross slip and its process in metals with vastly different intrinsic properties, temperature effects are not included. Increases in temperature will lower the critical stress for cross slip and at the dislocation-level, thermal fluctuations will aid small, short segments of a dislocation to locally overcome the energy barrier for cross slip [1, 26]. Compared to calculations via MD at finite temperatures, ranging from 350K – 715K, on Cu or Ni, the present calculations can be up to twice as high [32, 35, 36]. These MD studies model cross slip as a stochastic event through the use of transition state theory, a technique that has been applied to mesoscale simulation methods [10, 42, 43]. The PFDD technique has been extended to incorporate temperature effects on dislocation motion in HCP metals [68]. The role of thermal fluctuations on the kinetics is treated by incorporating a Langevin force term into the PFDD energy minimization procedure. Recently, a kinetic Monte Carlo algorithm was combined with

PFDD to account for temperature effects on the kinetics of dislocation motion in body centered cubic metals [69]. A similar method could be applied to FCC systems to study thermally activated cross slip of long dislocation(s).

In this work, we utilize the full anisotropic stiffness tensor to model the continuum elastic energy generated by screw dislocations. The major contribution of elastic anisotropy in our simulations is to lower the screw SFW. It should be noted that further aspects of dislocation behavior are affected by elastic anisotropy of the material. For example, atomistic and analytical models of the interaction energy field between dislocations and point defects were found to be in alignment only when elastic anisotropy is universally considered [70]. Such interactions are imperative to macroscale phenomena such as diffusion-controlled creep, and thus it is generally recommended that anisotropic elasticity be considered in computational models of dislocation-defect interactions.

6 Conclusions

In this work, we advanced the phase-field dislocation dynamics (PFDD) modeling technique to model cross slip of extended screw dislocations in eight face centered cubic (FCC) metals. The simulations feature elastic anisotropy (from experimental measurement or DFT), a high-fidelity representation of the entire DFT-calculated γ-surface, and an FCC discrete computational grid, so that all points lie on crystallographic planes. No additional input or rules or adjustable parameters is given. For reference, the equilibrium, zero stress stacking fault widths were calculated for eight FCC metals. The isotropic analytical SFW model agrees with the calculated SFWs, but the anisotropic analytical model overestimates the calculated values as the degree of elastic anisotropy rises. With PFDD, we demonstrate cross slip under an applied stress both in reaction to a hard obstacle and in an obstacle-free situation. The cross slip process observed follows the Friedel-Escaig mechanism, with constriction of the Shockley partials on the glide plane and subsequent glide on the cross slip plane. We show that the critical stress for cross slip scales directly with SFW and inversely with the ratio of the unstable to intrinsic

stacking fault, although there are exceptions. However without exception, the critical cross slip stress, either with or without an obstacle, scales proportionally with K_s, the elastic anisotropic energy coefficient for a screw dislocation. The strong influence of a factor that is relatively straightforward to calculate can benefit studies aiming to control cross slip in materials by material selection, temperature, or alloying. Simulations of dislocation behavior were conducted without the consideration of thermal fluctuations, and an investigation of temperature effects on glide and cross slip in FCC materials is left to future work. Finally, we demonstrated the ability of PFDD to predict cross slip under suitable conditions, which opens possibilities to study interactions of a dislocation or several dislocations with different types of obstacles and obstacle configurations.

7 Acknowledgments

This research was supported by funds from the UC National Laboratory Fees Research Program of the University of California, Grant Number L24GF7805. I. J. B. gratefully acknowledges support from the Office of Naval Research under contract N00014-21-1-2536. Use was made of computational facilities purchased with funds from the National Science Foundation (CNS-1725797) and administered by the Center for Scientific Computing (CSC). The CSC is supported by the California NanoSystems Institute and the Materials Research Science and Engineering Center (MRSEC; NSF DMR 2308708) at UC Santa Barbara. A.H. acknowledges support from the Physics and Engineering Models (PEM) Materials project within the Advanced Simulation and Computing (ASC) Program of the U.S. Department of Energy under contract 89233218CNA000001.

References

[1] P. M. Anderson, P. M. Anderson, J. P. Hirth, and J. Lothe, *Theory of dislocations*, eng, Third edition (Cambridge University Press, New York, NY, USA, 2017).

[2] L. Kubin and G. Canova, "The modelling of dislocation patterns", en, Scripta Metallurgica et Materialia **27**, 957 (1992).

[3] L. P. Kubin, "Dislocation Patterning during Multiple Slip of F.C.C. Crystals. A Simulation Approach", de, Physica Status Solidi (a) **135**, 433 (1993).

[4] R. Madec, B. Devincre, and L. Kubin, "Simulation of dislocation patterns in multislip", en, Scripta Materialia **47**, 689 (2002).

[5] S. Xia and A. El-Azab, "Computational modelling of mesoscale dislocation patterning and plastic deformation of single crystals", Modelling and Simulation in Materials Science and Engineering **23**, 055009 (2015).

[6] S.-D. Kim, J. Y. Park, S.-J. Park, J. H. Jang, J. Moon, H.-Y. Ha, C.-H. Lee, J.-Y. Kang, J.-H. Shin, and T.-H. Lee, "Direct observation of dislocation plasticity in high-Mn lightweight steel by in-situ TEM", en, Scientific Reports **9**, 15171 (2019).

[7] P. Jackson, "The formation of microbands by cross-slips", en, Scripta Metallurgica **17**, 199 (1983).

[8] W. D. Nix, J. C. Gibeling, and D. A. Hughes, "Time-dependent deformation of metals", Metallurgical Transactions A **16**, 2215 (1985).

[9] C. F. R. *. C. Déprés and M. C. Fivel, "Low-strain fatigue in aisi 316l steel surface grains: a three-dimensional discrete dislocation dynamics modelling of the early cycles i. dislocation microstructures and mechanical behaviour", Philosophical Magazine **84**, 2257 (2004).

[10] I. B. Z.Q. Wang and R. LeSar, "Slip band formation and mobile dislocation density generation in high rate deformation of single fcc crystals", Philosophical Magazine **88**, 1321 (2008).

[11] N. Mott, "CXVII. A theory of work-hardening of metal crystals", en, The London, Edinburgh, and Dublin Philosophical Magazine and Journal of Science **43**, 1151 (1952).

[12] P. R. Thornton, T. E. Mitchell, and P. B. Hirsch, "The dependence of cross-slip on stacking-fault energy in face-centred cubic metals and alloys", en, Philosophical Magazine **7**, 1349 (1962).

[13] G. Saada, "Cross-slip and work hardening of f.c.c. crystals", en, Materials Science and Engineering: A **137**, 177 (1991).

[14] P. Haasen, "Plastic deformation of nickel single crystals at low temperatures", en, Philosophical Magazine **3**, 384 (1958).

[15] G. Vanderschaeve, "Cross-slip of partial dislocations via the stair rod mode. the zigzag propagation of deformation microtwins in ordering alloys", physica status solidi (a) **100**, 59 (1987).

[16] S. Shen, P. Xie, C. Wu, J. Luo, H. Ye, and J. Chen, "Cross-slip of extended dislocations and secondary deformation twinning in a high-Mn TWIP steel", en, International Journal of Plasticity **175**, 103922 (2024).

[17] F. J. Humphreys and P. B. Hirsch, "The deformation of single crystals of copper and copper-zinc alloys containing alumina particles - ii. microstructure and dislocation-particle interactions", Proceedings of the Royal Society of London. A. Mathematical and Physical Sciences **318**, 73 (1970).

[18] Y. Matsukawa and G. S. Liu, "In situ TEM study on elastic interaction between a prismatic loop and a gliding dislocation", en, Journal of Nuclear Materials **425**, 54 (2012).

[19] J. S. Robach, I. M. Robertson, B. D. Wirth, and A. Arsenlis, "In-situ transmission electron microscopy observations and molecular dynamics simulations of dislocation-defect interactions in ion-irradiated copper", en, Philosophical Magazine **83**, 955 (2003).

[20] C. Singh, A. Mateos, and D. Warner, "Atomistic simulations of dislocation–precipitate interactions emphasize importance of cross-slip", Scripta Materialia **64**, 398 (2011).

[21] R. Peierls, "The size of a dislocation", Proceedings of the Physical Society **52**, 34 (1940).

[22] J. Bonneville, B. Escaig, and J. Martin, "A study of cross-slip activation parameters in pure copper", en, Acta Metallurgica **36**, 1989 (1988).

[23] S. H. Oh, M. Legros, D. Kiener, and G. Dehm, "In situ observation of dislocation nucleation and escape in a submicrometre aluminium single crystal", en, Nature Materials **8**, 95 (2009).

[24] J. Friedel, *Dislocations and Mechanical Properties of Crystals* (Wiley, New York, NY, 1957).

[25] B. Escaig, "Sur le glissement dévié des dislocations dans la structure cubique à faces centrées", Journal de Physique **29**, 225 (1968).

[26] W. Püschl, "Models for dislocation cross-slip in close-packed crystal structures: a critical review", en, Progress in Materials Science **47**, 415 (2002).

[27] G. Schoeck, "The cross-slip energy unresolved", en, Philosophical Magazine Letters **89**, 505 (2009).

[28] J. Bonneville and B. Escaig, "Cross-slipping process and the stress-orientation dependence in pure copper", en, Acta Metallurgica **27**, 1477 (1979).

[29] M. Duesbery, N. Louat, and K. Sadananda, "The mechanics and energetics of cross-slip", en, Acta Metallurgica et Materialia **40**, 149 (1992).

[30] R. Fleischer, "Cross slip of extended dislocations", en, Acta Metallurgica **7**, 134 (1959).

[31] T. Rasmussen, K. W. Jacobsen, T. Leffers, and O. B. Pedersen, "Simulations of the atomic structure, energetics, and cross slip of screw dislocations in copper", en, Physical Review B **56**, 2977 (1997).

[32] D. Mordehai, I. Kelson, and G. Makov, "Cross-slip and annihilation of screw dislocations in Cu: a molecular dynamics study", en, Materials Science and Engineering: A **400-401**, 37 (2005).

[33] K. Kang, J. Yin, and W. Cai, "Stress dependence of cross slip energy barrier for face-centered cubic nickel", en, Journal of the Mechanics and Physics of Solids **62**, 181 (2014).

[34] S. Xu, L. Xiong, Y. Chen, and D. L. McDowell, "Shear stress- and line length-dependent screw dislocation cross-slip in FCC Ni", en, Acta Materialia **122**, 412 (2017).

[35] E. Oren, E. Yahel, and G. Makov, "Kinetics of dislocation cross-slip: A molecular dynamics study", en, Computational Materials Science **138**, 246 (2017).

[36] G. Esteban-Manzanares, R. Santos-Güemes, I. Papadimitriou, E. Martínez, and J. LLorca, "Influence of the stress state on the cross-slip free energy barrier in Al: An atomistic investigation", en, Acta Materialia **184**, 109 (2020).

[37] W. P. Kuykendall, Y. Wang, and W. Cai, "Stress effects on the energy barrier and mechanisms of cross-slip in FCC nickel", en, Journal of the Mechanics and Physics of Solids **144**, 104105 (2020).

[38] B. Devincre, L. Kubin, and T. Hoc, "Collinear superjogs and the low-stress response of fcc crystals", en, Scripta Materialia **57**, 905 (2007).

[39] E. Martínez, J. Marian, A. Arsenlis, M. Victoria, and J. Perlado, "Atomistically informed dislocation dynamics in fcc crystals", en, Journal of the Mechanics and Physics of Solids **56**, 869 (2008).

[40] B. R. Ramírez, N. Ghoniem, and G. Po, "*Ab initio* continuum model for the influence of local stress on cross-slip of screw dislocations in fcc metals", en, Physical Review B **86**, 094115 (2012).

[41] P. Pauš, J. Kratochvíl, and M. Beneš, "A dislocation dynamics analysis of the critical cross-slip annihilation distance and the cyclic saturation stress in fcc single crystals at different temperatures", en, Acta Materialia **61**, 7917 (2013).

[42] A. M. Hussein, S. I. Rao, M. D. Uchic, D. M. Dimiduk, and J. A. El-Awady, "Microstructurally based cross-slip mechanisms and their effects on dislocation microstructure evolution in fcc crystals", en, Acta Materialia **85**, 180 (2015).

[43] M. Longsworth and M. Fivel, "The effect of stress on the cross-slip energy in face-centered cubic metals: A study using dislocation dynamics simulations and line tension models", en, Journal of the Mechanics and Physics of Solids **148**, 104281 (2021).

[44] Y. Wang, Y. Jin, A. Cuitiño, and A. Khachaturyan, "Nanoscale phase field microelasticity theory of dislocations: model and 3d simulations", Acta Materialia **49**, 1847 (2001).

[45] M. Koslowski, A. Cuitiño, and M. Ortiz, "A phase-field theory of dislocation dynamics, strain hardening and hysteresis in ductile single crystals", en, Journal of the Mechanics and Physics of Solids **50**, 2597 (2002).

[46] C. Shen and Y. Wang, "Incorporation of γ-surface to phase field model of dislocations: simulating dislocation dissociation in fcc crystals", en, Acta Materialia **52**, 683 (2004).

[47] A. Hunter, I. J. Beyerlein, T. C. Germann, and M. Koslowski, "Influence of the stacking fault energy surface on partial dislocations in fcc metals with a three-dimensional phase field dislocations dynamics model", en, Physical Review B **84**, 144108 (2011).

[48] H. Liu, S. Zheng, Y. Ni, and L. He, "Stress effects on interaction modes and cross-slip annihilation distance of screw dislocation interactions", en, Mechanics of Materials **197**, 105101 (2024).

[49] C. Albrecht, A. Kumar, S. Xu, A. Hunter, and I. J. Beyerlein, "Asymmetric equilibrium core structures of pyramidal-ii $<c+a>$ dislocations in ten hexagonal-close-packed metals", Phys. Rev. Mater. **5**, 043602 (2021).

[50] A. M. Roach, S. Xu, D. J. Luscher, D. S. Gianola, and I. J. Beyerlein, "Interaction of extended dislocations with nanovoid clusters", en, International Journal of Plasticity **168**, 103684 (2023).

[51] S. Zheng, D. Zheng, Y. Ni, and L. He, "Improved phase field model of dislocation intersections", npj Computational Materials **4**, 20 (2018).

[52] A. Ruffini, Y. Le Bouar, and A. Finel, "Three-dimensional phase-field model of dislocations for a heterogeneous face-centered cubic crystal", Journal of the Mechanics and Physics of Solids **105**, 95 (2017).

[53] X. Peng, A. Hunter, I. J. Beyerlein, R. A. Lebensohn, K. Dayal, and E. Martinez, "Non-orthogonal computational grids for studying dislocation motion in phase field approaches", en, Computational Materials Science **200**, 110834 (2021).

[54] L. T. W. Fey, A. Hunter, and I. J. Beyerlein, "Phase-field dislocation modeling of cross-slip", en, Journal of Materials Science **57**, 10585 (2022).

[55] A. Hunter and M. Koslowski, "Direct calculations of material parameters for gradient plasticity", Journal of the Mechanics and Physics of Solids **56**, 3181 (2008).

[56] S. Xu, Y. Su, and I. J. Beyerlein, "Modeling dislocations with arbitrary character angle in face-centered cubic transition metals using the phase-field dislocation dynamics method with full anisotropic elasticity", en, Mechanics of Materials **139**, 103200 (2019).

[57] C. Denoual, "Modeling dislocation by coupling Peierls–Nabarro and element-free Galerkin methods", en, Computer Methods in Applied Mechanics and Engineering **196**, 1915 (2007).

[58] H. Warlimont and W. Martienssen, eds., *Springer Handbook of Materials Data*, en, Springer Handbooks (Springer International Publishing, Cham, 2018).

[59] Y. Su, S. Xu, and I. J. Beyerlein, "Density functional theory calculations of generalized stacking fault energy surfaces for eight face-centered cubic transition metals", en, Journal of Applied Physics **126**, 105112 (2019).

[60] A. Hunter and I. Beyerlein, "Relationship between monolayer stacking faults and twins in nanocrystals", Acta Materialia **88**, 207 (2015).

[61] G. Schoeck, "The core structure, recombination energy and Peierls energy for dislocations in Al", en, Philosophical Magazine A **81**, 1161 (2001).

[62] A. Hunter, R. F. Zhang, and I. J. Beyerlein, "The core structure of dislocations and their relationship to the material γ-surface", en, Journal of Applied Physics **115**, 134314 (2014).

[63] J. G. Goiri and A. Van Der Ven, "MultiShifter: Software to generate structural models of extended two-dimensional defects in 3D and 2D crystals", en, Computational Materials Science **191**, 110310 (2021).

[64] B. A. Szajewski, A. Hunter, D. J. Luscher, and I. J. Beyerlein, "The influence of anisotropy on the core structure of Shockley partial dislocations within FCC materials", Modelling and Simulation in Materials Science and Engineering **26**, 015010 (2018).

[65] P. Landau, D. Mordehai, A. Venkert, and G. Makov, "Universal strain–temperature dependence of dislocation structures at the nanoscale", en, Scripta Materialia **66**, 135 (2012).

[66] J. Gubicza, N. Q. Chinh, J. L. Lábár, Z. Hegedűs, C. Xu, and T. G. Langdon, "Microstructure and yield strength of severely deformed silver", Scripta Materialia **58**, 775 (2008).

[67] W. Püschl and G. Schoeck, "Calculation of cross-slip parameters in f.c.c. crystals", en, Materials Science and Engineering: A **164**, 286 (1993).

[68] C. Albrecht, I. J. Beyerlein, and M. R. Jones, "Temperature dependent phase field dislocation dynamics model", en, European Journal of Mechanics - A/Solids **100**, 104987 (2023).

[69] X. Peng, N. Mathew, I. J. Beyerlein, E. Martinez, and A. Hunter, "A combined kinetic Monte Carlo and phase field approach to model thermally activated dislocation motion", en, Computational Materials Science **230**, 112490 (2023).

[70] E. Clouet, S. Garruchet, H. Nguyen, M. Perez, and C. S. Becquart, "Dislocation interaction with c in α-fe: a comparison between atomic simulations and elasticity theory", Acta Materialia **56**, 3450 (2008).

8 Appendices

8.1 Values of γ_{gsf} for eight FCC metals

Tables of Fourier series terms used to parameterize the γ-surface for eight FCC metals, using Equation 8 for γ_{gsf} given above:

A_{nm} / B_{op}	sin / cos	n / o	m / p
-1.002806	cos	3	-1
-1.159734	cos	3	1
-1.170065	cos	2	4
-1.210744	cos	1	-5
-1.236685	cos	2	-4
-1.301471	cos	1	5
-1.861596	sin	2	-4
1.909977	sin	3	1
-1.911371	sin	3	-1
1.927822	sin	1	-5
1.933037	sin	2	4
-1.934661	sin	1	5
3.153347	cos	0	-4
3.22774	cos	2	2
3.404015	cos	2	-2
5.731787	sin	0	-4
6.175411	sin	2	2
-6.280206	sin	2	-2
-15.54031	cos	2	0
-15.95516	cos	1	3
-16.0704	cos	1	-3
-57.00842	cos	0	-2
-58.49648	cos	1	-1
-58.65317	cos	1	1
93.85783	sin	0	-2
97.2037	sin	1	1
-97.20805	sin	1	-1
220.1973	cos	0	0

Table 4: Ag

A_{nm} / B_{op}	sin / cos	n / o	m / p
-1.346036	cos	3	-1
-1.390111	cos	1	5
-1.400701	cos	2	-4
-1.414934	cos	3	1
-1.420884	cos	1	-5
-1.451948	cos	2	4
-1.921959	sin	3	-1
1.935711	sin	3	1
-2.052228	sin	2	-4
2.053703	sin	2	4
-2.067353	sin	1	5
2.081598	sin	1	-5
3.584475	cos	0	-4
3.598583	cos	2	2
3.621059	cos	2	-2
-7.606874	sin	2	-2
7.653461	sin	2	2
7.671776	sin	0	-4
-12.85583	cos	2	0
-13.68223	cos	1	3
-13.71983	cos	1	-3
-45.58045	cos	1	-1
-45.60515	cos	1	1
-46.37485	cos	0	-2
71.42202	sin	1	1
-71.45345	sin	1	-1
73.43161	sin	0	-2
176.3105	cos	0	0

Table 5: Au

A_{nm} / B_{op}	sin / cos	n / o	m / p
-1.278417	cos	1	-5
-1.293769	cos	3	1
-1.33398	cos	3	-1
-1.406927	cos	1	5
-1.467355	cos	2	-4
-1.50688	cos	2	4
-2.13134	sin	2	-4
2.175776	sin	3	1
2.295692	sin	2	4
2.344248	sin	1	-5
-2.411782	sin	3	-1
-2.430872	sin	1	5
4.074517	cos	0	-4
4.377277	cos	2	2
4.398633	cos	2	-2
8.329971	sin	0	-4
-9.01989	sin	2	-2
9.041115	sin	2	2
-22.1248	cos	2	0
-22.74947	cos	1	3
-22.91647	cos	1	-3
-104.3822	cos	0	-2
-105.7677	cos	1	-1
-105.8889	cos	1	1
165.3755	sin	0	-2
-170.1183	sin	1	-1
170.1881	sin	1	1
379.3413	cos	0	0

Table 6: Cu

A_{nm} / B_{op}	sin / cos	n / o	m / p
-1.378321	sin	3	-3
1.423232	sin	3	3
-2.04229	cos	4	0
-2.252283	cos	2	6
-2.279482	cos	2	-6
-8.000332	cos	1	5
-8.035971	cos	1	-5
-8.529464	cos	2	-4
-8.580177	cos	2	4
-8.98783	cos	3	1
-9.049285	cos	3	-1
9.541984	cos	0	-4
10.72661	cos	2	-2
10.7509	cos	2	2
12.00601	sin	1	-5
-12.0258	sin	1	5
-12.26825	sin	2	-4
12.37218	sin	2	4
12.62713	sin	3	1
-12.63649	sin	3	-1
36.10445	sin	0	-4
36.69329	sin	2	2
-36.72283	sin	2	-2
-124.7591	cos	1	-3
-124.7676	cos	1	3
-129.068	cos	2	0
-165.6069	cos	0	-2
-168.4587	sin	1	-1
168.6006	sin	1	1
169.0856	sin	0	-2
-171.323	cos	1	1
-171.4216	cos	1	-1
911.255	cos	0	0

Table 7: Ir

A_{nm} / B_{op}	sin / cos	n / o	m / p
-1.105086	cos	2	6
-1.193741	cos	2	-6
2.092111	cos	4	0
-2.646377	cos	2	4
-2.663776	cos	3	1
-2.674259	cos	1	-5
-2.678564	cos	1	5
-2.727462	cos	2	-4
-2.812001	cos	3	-1
3.8734	sin	1	-5
3.886615	sin	3	1
-3.894146	sin	1	5
3.942342	sin	2	4
-3.94903	sin	2	-4
-3.97842	sin	3	-1
4.727294	cos	0	-4
4.992983	cos	2	-2
5.025235	cos	2	2
16.11839	sin	0	-4
-16.5071	sin	2	-2
16.51017	sin	2	2
-38.94427	cos	1	3
-39.01026	cos	1	-3
-39.16039	cos	2	0
-156.1637	cos	0	-2
-156.8333	cos	1	-1
-156.9383	cos	1	1
-223.0412	sin	1	-1
223.1167	sin	1	1
223.4281	sin	0	-2
587.2152	cos	0	0

Table 8: Ni

A_{nm} / B_{op}	sin / cos	n / o	m / p
1.356969	cos	2	-2
1.416386	cos	2	2
1.689847	cos	0	-4
-1.70022	cos	2	-4
-1.739534	cos	2	4
-1.743498	cos	3	1
-1.757776	cos	1	-5
-1.790147	cos	3	-1
-1.855397	cos	1	5
-2.52023	sin	2	-4
-2.664205	sin	1	5
2.675938	sin	1	-5
2.683672	sin	2	4
2.692878	sin	3	1
-2.756335	sin	3	-1
9.18885	sin	0	-4
-9.204379	sin	2	-2
9.319446	sin	2	2
-25.90094	cos	1	3
-25.91209	cos	1	-3
-26.50037	cos	2	0
-90.16154	cos	1	1
-90.20001	cos	1	-1
-91.07588	cos	0	-2
112.4729	sin	1	1
-112.4891	sin	1	-1
114.5172	sin	0	-2
357.1646	cos	0	0

Table 9: Pd

A_{nm} / B_{op}	sin / cos	n / o	m / p
1.010182	sin	4	2
1.017681	sin	3	5
-1.05246	sin	3	-5
1.071898	cos	3	3
1.074655	cos	3	-3
-1.078193	sin	1	7
1.083931	cos	2	2
1.111594	sin	1	-7
1.164061	cos	2	-2
1.61444	cos	0	-4
-1.822556	cos	2	6
-1.924785	cos	2	-6
-1.971383	cos	4	0
-3.37071	cos	2	-4
-3.382113	cos	2	4
-3.564238	cos	3	1
-3.566597	cos	3	-1
-3.593568	cos	1	-5
-3.600463	cos	1	5
4.284049	sin	3	1
-4.290886	sin	3	-1
4.371351	sin	2	4
4.443626	sin	1	-5
-4.455881	sin	2	-4
-4.500909	sin	1	5
17.92025	sin	2	2
-17.98274	sin	2	-2
18.261	sin	0	-4
-31.20643	cos	2	0
-31.80146	cos	1	-3
-31.84817	cos	1	3
65.78043	sin	1	1
-65.84877	sin	1	-1
66.10318	sin	0	-2
-87.35806	cos	1	-1
-87.38135	cos	1	1
-89.68651	cos	0	-2
379.7967	cos	0	0

Table 10: Pt

A_{nm} / B_{op}	sin / cos	n / o	m / p
-1.073984	cos	2	-6
-1.188377	cos	4	0
1.357898	cos	8	0
-1.389501	cos	2	6
-4.490554	cos	2	4
-4.827993	cos	2	-4
-4.831574	cos	3	1
-4.834101	cos	1	-5
-4.900389	cos	1	5
-5.190815	cos	3	-1
6.729313	cos	0	-4
7.017633	sin	1	-5
7.132479	sin	3	1
7.183771	sin	2	4
-7.210314	sin	3	-1
-7.24299	sin	2	-4
-7.267438	sin	1	5
7.931369	cos	2	2
8.062793	cos	2	-2
23.69495	sin	0	-4
23.71257	sin	2	2
-23.90637	sin	2	-2
-88.16433	cos	1	-3
-88.26113	cos	1	3
-88.26503	cos	2	0
-138.9095	cos	0	-2
-141.752	cos	1	1
-141.9362	cos	1	-1
-176.5185	sin	1	-1
176.5235	sin	1	1
178.9287	sin	0	-2
695.5565	cos	0	0

Table 11: Rh

8.2 Comparison of calculated equilibrium SFW to analytical models

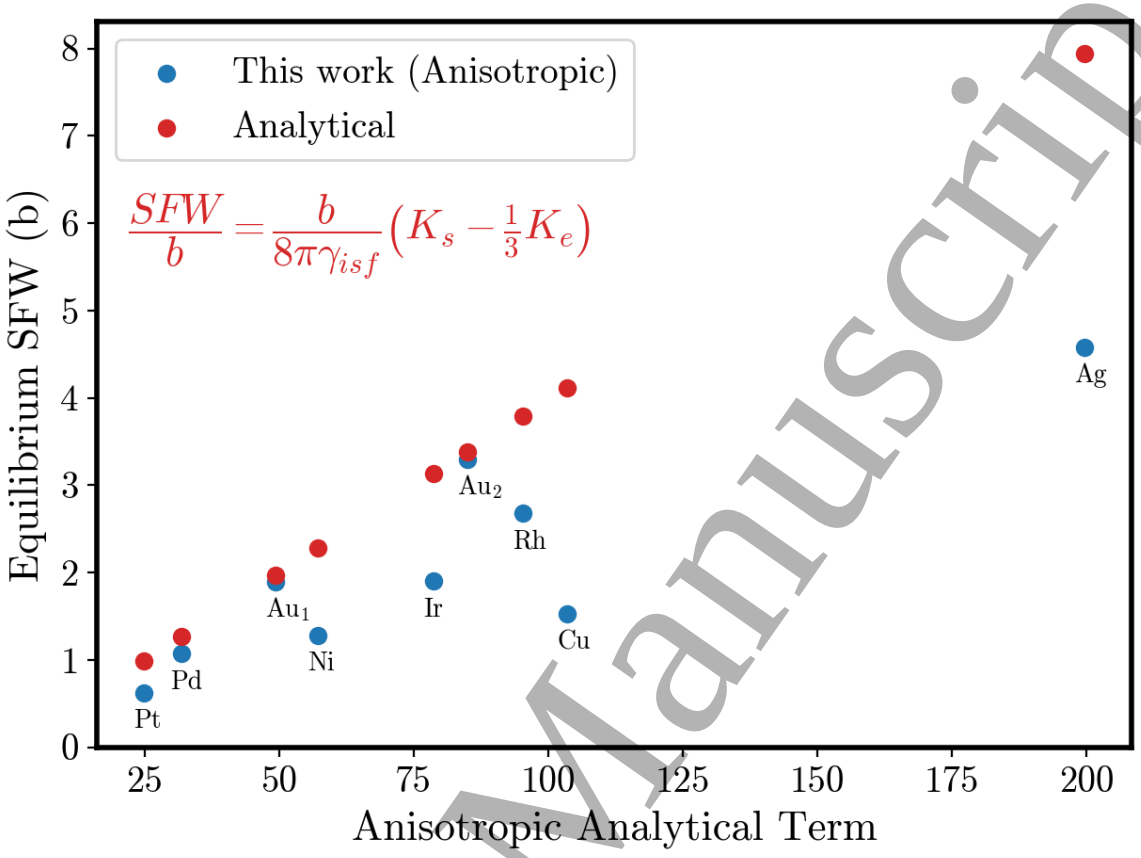

Figure 11: Equilibrium SFW in terms of Burgers vector for eight FCC metals calculated using PFDD, plotted over an elastically anisotropic analytical model for SFW of an extended FCC screw dislocation (right side of above equation) [1]. Predicted analytical SFW values plotted in red.

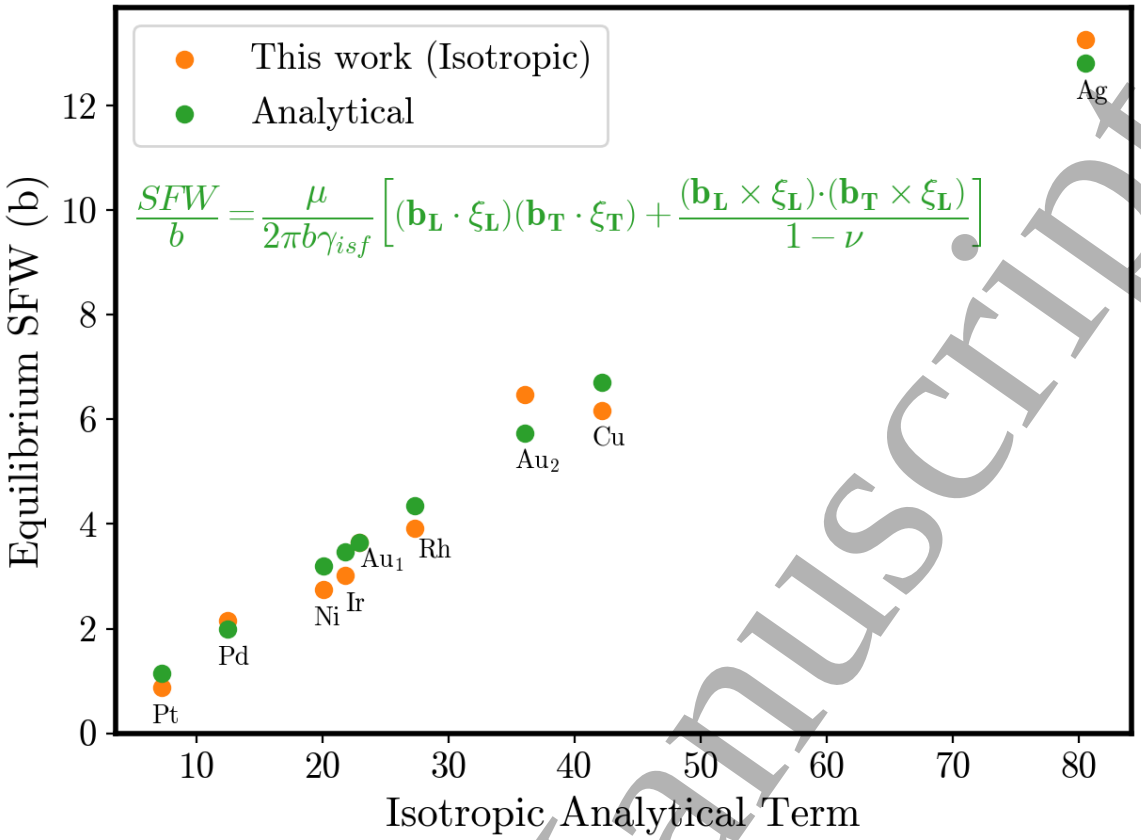

Figure 12: Equilibrium SFW in terms of Burgers vector for eight FCC metals calculated using PFDD, plotted over an elastically isotropic analytical model for SFW of an extended FCC screw dislocation (right side of above equation) [1]. Predicted analytical SFW values plotted in green.